

Modeling Multivariable High-resolution 3D Urban Microclimate Using Localized Fourier Neural Operator

Shaoxiang Qin^{1,2}, Dongxue Zhan¹, Dingyang Geng¹, Wenhui Peng¹, Geng Tian¹, Yurong Shi¹, Naiping Gao³, Xue Liu², and Liangzhu (Leon) Wang^{1,*}

¹Concordia University, Centre for Zero Energy Building Studies, Department of Building, Civil and Environmental Engineering, Montreal, H3G 1M8, Canada

²McGill University, School of Computer Science, Montreal, H3A 0E9, Canada

³Tongji University, School of Mechanical Engineering, Shanghai, 200092, China

*leon.wang@concordia.ca

ABSTRACT

Accurate urban microclimate analysis with wind velocity and temperature is vital for energy-efficient urban planning, supporting carbon reduction, enhancing public health and comfort, and advancing the low-altitude economy. However, traditional computational fluid dynamics (CFD) simulations that couple velocity and temperature are computationally expensive. Recent machine learning advancements offer promising alternatives for accelerating urban microclimate simulations. The Fourier neural operator (FNO) has shown efficiency and accuracy in predicting single-variable velocity magnitudes in urban wind fields. Yet, for multivariable high-resolution 3D urban microclimate prediction, FNO faces three key limitations: blurry output quality, high GPU memory demand, and substantial data requirements. To address these issues, we propose a novel localized Fourier neural operator (Local-FNO) model that employs local training, geometry encoding, and patch overlapping. Local-FNO provides accurate predictions for rapidly changing turbulence in urban microclimate over 60 seconds, four times the average turbulence integral time scale, with an average error of 0.35 m/s in velocity and 0.30 °C in temperature. It also accurately captures turbulent heat flux represented by the velocity-temperature correlation. In a 2 km by 2 km domain, Local-FNO resolves turbulence patterns down to a 10 m resolution. It provides high-resolution predictions with 150 million feature dimensions on a single 32 GB GPU at nearly 50 times the speed of a CFD solver. Compared to FNO, Local-FNO achieves a 23.9% reduction in prediction error and a 47.3% improvement in turbulent fluctuation correlation.

1 Introduction

As the world moves towards ambitious carbon neutrality targets by 2050, the built environment plays a critical role in achieving global sustainability. The building sector, accounting for 30% of global energy consumption and 26% of energy-related greenhouse gas (GHG) emissions [1], is a significant factor in this sustainability transition. Accurate modeling and representation of the urban microclimate have become essential, providing city planners and policymakers with data crucial for designing energy-efficient, sustainable urban areas. The urban microclimate encompasses highly localized environmental conditions influenced by the surrounding infrastructure, with spatial resolutions from 1 mm to 1 km. Unlike rural environments, urban microclimates exhibit distinct variations in wind speed, wind direction, and air temperature. These localized climate variations profoundly impact building energy efficiency, outdoor thermal comfort, and airflow dynamics within cities [2]. For instance, the urban heat island effect—characterized by elevated temperatures in urban areas—amplifies cooling demands, reducing the overall energy efficiency of buildings [3]. Additionally, as innovations like drone delivery and urban air mobility emerge, a comprehensive understanding of urban airflow and turbulence becomes integral to sustainable city planning and development in this new low-altitude economy.

Urban microclimate research primarily utilizes field measurements, experimental methods, and numerical simulations. Field measurements capture temporally varied data such as air temperature, relative humidity, wind speed, and wind direction, offering a realistic view of the daily variations in weather conditions across urban areas [4, 5, 3]. Additionally, advanced tools such as helicopter and satellite thermal imaging aid in gathering temperature distribution data across urban landscapes, thereby enhancing understanding at a broader spatial scale [6]. Concurrently, wind tunnel experiments—a physical analysis technique extensively used in urban airflow studies—enable the simulation and analysis of air movement under controlled environmental conditions [7]. Despite their contributions, each of these experimental methods has limitations. For example, wind tunnel studies have historically concentrated on airflow, with fewer investigations into the thermal conditions and radiation effects within urban canyons [8, 9, 10]. Although some experiments incorporate thermal buoyancy, the emphasis remains on temperature and wind velocity within generic building models or single-street canyon setups. These simplified configurations

often omit essential variables, such as solar radiation and shading dynamics, failing to reflect the complex geometries and interactions present in real urban environments [11]. Furthermore, experimental techniques generally capture data from only a limited number of spatial points, providing a narrower perspective than the comprehensive coverage possible through numerical simulations. This limitation highlights the need for multi-scale approaches that integrate experimental insights with the broader, more detailed outputs achievable in simulation-based studies.

Over recent decades, advancements in computational resources have made numerical simulations, particularly computational fluid dynamics (CFD), increasingly popular for urban microclimate assessment [12, 13, 14, 15, 16, 17]. CFD enables detailed analysis of heat and mass transfer interactions with urban features like buildings and trees, supporting high-resolution simulations that couple velocity and temperature fields. This flexibility allows CFD to model urban microclimates across different scales, from entire cities [18, 13] to street level [19, 20]. However, CFD simulations necessitate a detailed, high-resolution representation of urban geometry, which includes accurately modeling the shapes, sizes, and spatial arrangements of buildings, vegetation, and other urban elements. Precise boundary conditions for all relevant flow variables, such as temperature, wind velocity, humidity, and solar radiation, are also essential to capture the dynamic interactions within urban environments accurately. Additionally, CFD simulations demand substantial computational resources to handle the high volumes of data and complex calculations required to resolve fine-scale processes across large domains. These requirements make CFD a resource-intensive approach, particularly for large urban-scale simulations that may require advanced computational infrastructure and optimization techniques to manage the extensive computational load effectively [21, 22].

With the recent progress in artificial intelligence, deep learning models, particularly deep neural networks, have demonstrated potential as more efficient surrogate models for solving partial differential equations (PDEs) than traditional numerical methods. After being trained on PDE equations or solution data, neural networks can quickly predict PDE solutions for unseen cases. The two main deep learning paradigms for solving PDEs are learning physics-informed models and purely data-driven models. Physics-informed models, like physics-informed neural networks (PINNs) [23, 24], use physics-based loss functions and optional data observations to guide their training. This physics loss introduces knowl-

edge of the underlying PDEs, helping to produce more accurate predictions in data-limited or even data-free scenarios. Like traditional numerical solvers, physics-informed models rely on the governing PDE equations. In contrast, pure data-driven models do not require any physics knowledge and can be trained solely on historical or synthetic data [25, 26, 27]. As a trade-off, they tend to require a larger amount of training data compared to physics-informed models. One significant advantage of pure data-driven models is their ability to overcome the limitations of traditional physical models, which often rely on simplified assumptions that may not fully capture the complexities of real-world natural dynamics. Recent advanced deep learning weather models, such as Pangu [28] and GraphCast [29], can be trained end-to-end on weather data and have demonstrated the ability to produce more accurate predictions than the leading numerical weather models. NeuralGCM [30] further improves forecasting performance through the integration of machine learning components and a differentiable solver.

Common deep learning models, such as convolutional neural networks (CNNs) [31], graph neural networks (GNNs) [32], and transformers [33], are designed for spatially or temporally discrete data. These models are trained on fixed-resolution datasets and cannot generalize to other spatial or temporal points. This restriction poses challenges in modeling continuous natural processes like fluid dynamics. To address this, neural operators [25, 26] have been developed as resolution-invariant models for scientific machine learning. Neural operators approximate operators—mappings between continuous functions—and can make predictions across different resolutions, even when trained on fixed-resolution data. Among the neural operators, Fourier neural operator (FNO) [34] demonstrates superior accuracy and efficiency and have been applied to a range of fields, such as modeling weather [35], fluid turbulence [36], materials [37], smectic waves [38], and plasma [39]. Unlike traditional neural networks like CNN, which are parameterized in the physical domain, most of the parameters in FNO are defined in the Fourier domain. This enables FNO to learn resolution-invariant representations from the data. Additionally, the Fourier transformation in FNO functions similarly to a reduced-order model, as turbulence data typically concentrates energy in low-frequency modes [40]. FNO commonly truncates high-frequency modes to improve memory and time efficiency during training and predicting. Recently, FNO has been demonstrated to be an effective approach for modeling velocity magnitude field in urban microclimate [41].

This work focuses on making fast and accurate predictions for multivariable high-resolution 3D urban microclimate, specifically, the three directional wind velocity and temperature. Previous research is limited to predicting the velocity magnitude (one variable) in urban wind fields [41]. When applied to multivariable urban microclimate prediction in complex urban environments, vanilla FNO faces three critical limitations: blurry output quality, extensive GPU memory usage, and substantial data demands. First, FNO’s predictions often appear blurry because urban microclimate with temperature differences involves complex physical processes, resulting in intricate small-scale features in the flow field. The truncation of high-frequency modes in each Fourier layer limits FNO’s capacity to capture these small-scale features accurately. Second, FNO’s GPU memory usage during prediction scales nearly proportionally with the total grid number of the wind field data. Given the high dimensionality of multivariable 3D data, FNO often requires excessive memory that may exceed available resources. Third, the curse of dimensionality poses a significant challenge for modeling complex physical processes with machine learning methods. In multivariable 3D microclimate simulations, CFD data dimensions—including three directional wind velocity and temperature across all grids—can reach hundreds of millions, while only thousands of time steps may be available for training. The dataset becomes extremely sparse in such a high-dimensional space, making the machine learning model easily overfit and perform poor generalization.

To overcome these limitations, we introduce the localized Fourier neural operator (Local-FNO), a novel approach for learning and predicting multivariable high-resolution 3D urban microclimate. The core design is to train the FNO on smaller, local patches of the domain rather than applying it to the entire domain at once. This local training strategy addresses all three limitations. First, Local-FNO effectively captures small-scale features in the wind field. With the same number of Fourier modes, the smaller domain size produces shorter Fourier wavelengths, allowing Local-FNO to represent finer details than FNO. Second, Local-FNO makes independent predictions for each small patch at every time step, reducing peak memory usage. This approach also allows for parallel predicting when multiple GPUs are available. Third, by dividing the entire domain into smaller patches and training a shared Local-FNO on each, we reduce the data dimensionality and increase the number of training samples, thus lowering the data requirements and enhancing FNO’s generalization ability. Two methods are further incorporated into Local-FNO to enhance its performance and counteract the side effects of local training: geometry

encoding and patch overlapping. Geometry encoding informs Local-FNO with local building geometries using signed distance functions. Patch overlapping allows wind flow to interact across neighboring patches, minimizing discontinuities at the patch boundaries. With these designs, Local-FNO is capable of producing accurate and fast predictions for multivariable, high-resolution 3D urban microclimate. Its effectiveness and efficiency are validated through comprehensive evaluations.

Several prior studies have aimed to enhance neural operators' ability to capture small-scale features and sharpen predictions beyond FNO. U-FNO [42] and IU-FNO [36] incorporate a U-Net structure into FNO. U-Net [43] employs a U-shaped architecture with downsampling and upsampling to capture multiscale features. HANO [44] decomposes the input-output mapping into hierarchical levels and applies self-attention across these levels to improve multiscale feature capture. LNO [45] combines convolution in physical space with linear transformations in Legendre spectral space to learn local operators from PDE data. However, unlike FNO, these models [42, 36, 44, 45] lack resolution invariance due to their reliance on convolutions or attentions within discrete spatial domains. Some methods can retain FNO's resolution-invariant property. For instance, a local integral kernel [46] is introduced to replace discrete convolution, achieving resolution-invariant local convolution by applying a continuous convolutional kernel approximated by summing over a fixed set of triangular functions on discrete data points. Compared to this local integral kernel, our proposed Local-FNO demonstrates that Fourier modes defined over local regions are also effective at capturing resolution-invariant local features with a more straightforward implementation. Other methods include PDE-Refiner [47], which uses a denoising diffusion model to refine predictions from various machine learning models, enhancing their performance on non-dominant frequencies, although it is less effective for FNO than other models. SpecB-FNO [48] enhances FNO's prediction of non-dominant frequencies by sequentially training multiple FNOs, with each learning to predict the residual of its predecessor. However, its improvement is limited when FNO uses relatively few Fourier modes. All methods mentioned above, except for LNO, require training on the entire domain of PDE data, making them unsuitable for the extremely high-dimensional data in this study given limited computational resources.

2 Methodology

2.1 Numerical simulations

The airflow and temperature data generated by City Fast Fluid Dynamics (CityFFD) serve as training and testing data for FNO and Local-FNO models. By employing a semi-Lagrangian approach and fractional stepping method with various novel numerical schemes, CityFFD enhances model accuracy and reduces computational costs [49, 14]. A large eddy simulation (LES) model is implemented in CityFFD to capture turbulence within the atmospheric boundary layer [16]. CityFFD integrates a fourth-order numerical interpolation scheme to minimize numerical dissipation and dispersion errors, even on coarse grids. Developed with CUDA-C++ for GPU processing, CityFFD is designed to predict local microclimate features and model large-scale urban aerodynamics. Recent studies have shown that CityFFD can effectively model urban-scale building scenarios, with its fundamental theory detailed in prior research [13, 14]. Previous studies have applied CityFFD in urban areas to evaluate wind and thermal scenarios. CityFFD can also integrate with the Weather Research and Forecasting Model (WRF) and couple with building energy models [50, 51]. A series of validation cases, comparing CityFFD results with wind tunnel and real urban data, have been conducted under both isothermal and non-isothermal conditions. These validations demonstrate that CityFFD performs well in predicting airflow and air temperature.

CityFFD solves the continuity, momentum, and energy equations presented as:

$$\begin{aligned}\nabla \cdot \vec{U} &= 0 \\ \frac{\partial \vec{U}}{\partial t} + (\vec{U} \cdot \nabla) \vec{U} &= -\nabla p + \left(\frac{1}{Re} + \nu_t \right) \nabla^2 \vec{U} - \frac{Gr}{Re^2} \theta \\ \frac{\partial \theta}{\partial t} + (\vec{U} \cdot \nabla) \theta &= \left(\frac{1}{Re \cdot Pr} + \alpha_t \right) \nabla^2 \theta ,\end{aligned}\tag{1}$$

where \vec{U} , θ , and p , Re , Gr , Pr , ν_t , and α_t represent the velocity vector, temperature, pressure, Reynolds number, Grashof number, Prandtl number, turbulent viscosity, and turbulent thermal diffusivity, respectively.

The advection terms in Equation 1 are solved using a Lagrangian approach, which calculates the air temperature and wind velocity at position S_c^{n+1} based on the values of \vec{U} and θ at position S_c^n , as shown

in Equation 2:

$$S_c = \vec{U} dt \rightarrow S_c^n \approx S_c^{n+1} - \vec{U} \Delta t . \quad (2)$$

The turbulent viscosity is calculated by the following equation:

$$\nu_t = (c_s \Delta)^2 |S| , \quad (3)$$

where c_s is the Smagorinsky constant, typically ranging from 0.1 to 0.24, Δ is the filter width, and S is the large-scale strain rate. CityFFD employs a fourth-order interpolation scheme to model airflow on coarse grids and reduce high dissipation errors. Detailed methodology can be found in earlier work [52].

2.2 Data description

The studied building cluster is located in downtown Montreal, covering a $2 \text{ km} \times 2 \text{ km}$ area with 274 buildings, the tallest of which is 200 m. Buildings are densely distributed in the central $1.5 \text{ km} \times 1.5 \text{ km}$ section. The total computational domain is $4 \text{ km} \times 4 \text{ km}$ with a height of 1 km, as demonstrated in Figure 1. It consists of 54 million grids, with the minimum grid size near buildings being $4 \text{ m} \times 4 \text{ m}$ horizontally and 1 m vertically. Vertical boundaries of the domain function as inlets or outlets, depending on wind direction, while the ground boundary is set as a wall and the top as symmetry. Building surface temperatures, calculated by the City Building Energy Model (CityBEM) [12], serve as boundary conditions in CityFFD simulations. Inlet boundary conditions were taken from Dorval airport weather station, located 13 km from the studied area. Simulations were conducted for July 16, 2013, at 17:00, with an air temperature of $30.7 \text{ }^\circ\text{C}$, wind speed of 4.16 m/s, and wind direction of 23° from y -axis toward x -axis. The time step was set at 0.2 s.

Validation for this case has been studied in previous literature [11], showing an RMSE of $0.97 \text{ }^\circ\text{C}$ for air temperature and 0.257 m/s for wind velocity. The validation was conducted over two consecutive days during a heatwave, using onsite measurements documented by Environment and Climate Change Canada as part of a temporary field campaign in the summer of 2013.

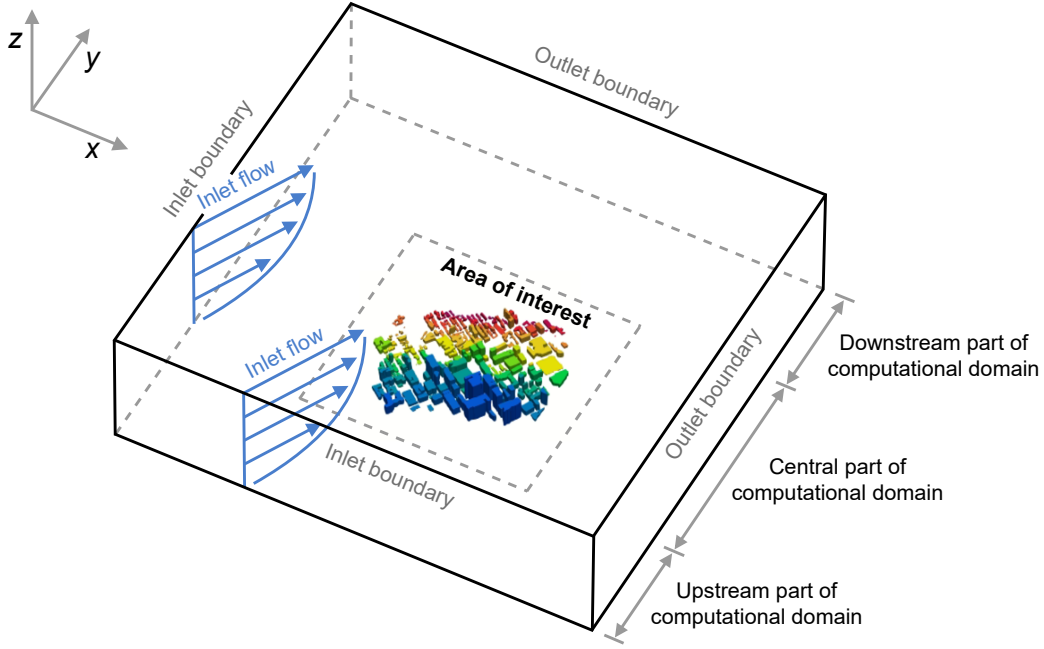


Figure 1. Computational domain for CFD simulation

2.3 Neural operators and Fourier neural operator

Neural operators are designed to learn the mapping between input and output functions defined in continuous spaces. Below, we introduce the problem settings for neural operators as established in prior research [34, 53]. Let $D \subset \mathbb{R}^d$ be a bounded domain with spatial dimension $d \in \mathbb{N}$, where, for example, $d = 3$ represents a 3D space. Consider $a \in \mathcal{A}(D; \mathbb{R}^{d_a})$ as the input function $a : D \rightarrow \mathbb{R}^{d_a}$, which has $d_a \in \mathbb{N}$ components, and $u \in \mathcal{U}(D; \mathbb{R}^{d_u})$ as the output function $u : D \rightarrow \mathbb{R}^{d_u}$, which has $d_u \in \mathbb{N}$ components. d_a and d_u can be considered as the variable dimensions defined on the input space and output space, respectively. Both $\mathcal{A}(D; \mathbb{R}^{d_a})$ and $\mathcal{U}(D; \mathbb{R}^{d_u})$ are Banach spaces, and let $\mathcal{G}^\dagger : \mathcal{A}(D; \mathbb{R}^{d_a}) \rightarrow \mathcal{U}(D; \mathbb{R}^{d_u})$ denote the true operator between these spaces. The goal of operator learning is to approximate the true operator \mathcal{G}^\dagger by learning a model \mathcal{G}_θ , parameterized by θ , using a finite set of discretized input-output samples from \mathcal{G}^\dagger . The neural operator proposed by Li et al. [54] is defined as:

$$\mathcal{G}_\theta = \mathcal{Q} \circ \mathcal{L}_L \circ \mathcal{L}_{L-1} \circ \cdots \circ \mathcal{L}_1 \circ \mathcal{P}, \quad (4)$$

where $L \in \mathbb{N}$ is the depth of the model. The mapping begins with the lifting operator $\mathcal{Q} : \mathcal{A}(D; \mathbb{R}^{d_a}) \rightarrow \mathcal{U}(D; \mathbb{R}^{d_v})$, which raises the input channels from d_a to d_v . The number of channels remains d_v through

all intermediate layers and is projected back to the output channels using the projection operator $\mathcal{P} : \mathcal{U}(D; \mathbb{R}^{d_v}) \rightarrow \mathcal{U}(D; \mathbb{R}^{d_u})$. Both \mathcal{Q} and \mathcal{P} are pointwise operators, meaning they act independently at each point in the d -dimensional space. $\mathcal{L}_1, \mathcal{L}_2, \dots, \mathcal{L}_L$ represent nonlinear operator layers, which are key to achieving the mapping between continuous spaces. For $\ell \in L$, the mapping $\mathcal{L}_\ell : \mathcal{U}(D; \mathbb{R}^{d_v}) \rightarrow \mathcal{U}(D; \mathbb{R}^{d_v})$ keeps the channels d_v .

In this work, the nonlinear operator layer is defined as follows:

$$\mathcal{L}_\ell(v)(x) = \sigma(\mathcal{M}_\ell((\mathcal{K}(\theta_\ell)v)(x)) + W_\ell v(x) + b_\ell(x) + v(x)) , \quad (5)$$

where $x \in \mathbb{R}^d$ is the spatial coordinate and $v \in \mathcal{U}(D; \mathbb{R}^{d_v})$ is the function in the intermediate layers. \mathcal{L}_ℓ consists of a kernel operator $(\mathcal{K}(\theta_\ell)v)(x)$, a pointwise nonlinear feedforward network \mathcal{M}_ℓ , a pointwise affine mapping $W_\ell v(x) + b_\ell(x)$, an identity mapping $v(x)$, and a nonlinear activation function σ . In contrast to its original definition [54], we incorporate two design modifications frequently used in the latest research: identity mappings and point-wise feedforward neural networks (FFNs). Identity mappings [55] enable deep neural networks to scale a large number of layers and have demonstrated effectiveness in neural operators [56]. The point-wise FFN, inspired by the transformer’s architecture [57], enhances the information interaction between channels.

Fourier neural operator [34] is a specialized type of neural operator with advantageous performance in solving PDEs. The kernel operator in FNO is defined as a complex linear transformation in Fourier space, specifically:

$$(\mathcal{K}(\theta)v)(x) = \mathcal{F}^{-1}(\mathcal{R}_\theta(k) \cdot \mathcal{F}(v)(k))(x) . \quad (6)$$

Here, \mathcal{F} and \mathcal{F}^{-1} represent the Fourier transform and inverse Fourier transform, respectively. $k \in \mathbb{Z}^d$ is the complex index in Fourier space, and $\mathcal{R}_\theta(k) \in \mathbb{C}^{d_v \times d_v}$ is a complex matrix that performs linear mapping in this space. In FNO, only the kernel operator \mathcal{K} is not a pointwise operator. The kernel operator enables information interaction across all spatial locations and acts as a continuous global convolution kernel.

In practice, FNO is trained on samples defined on discretized grids over D . The Fourier transform

\mathcal{F} and inverse \mathcal{F}^{-1} are computed using the fast Fourier transform (FFT) algorithm [58]. Since FFT operates only on structured grids, FNO can only use data that is either defined on or can be converted to a structured grid [59]. Pointwise mappings \mathcal{Q} , \mathcal{P} , and \mathcal{M} are typically implemented using a multilayer perceptron (MLP) [60] with one hidden layer. These mappings operate independently on each grid point.

For inputs defined on structured grids, the transformed inputs in the Fourier domain retain the same structured grids with an identical number of grid points. Each grid index k in the Fourier domain, referred to as a mode, corresponds to a sinusoidal wave in the spatial domain with a specific frequency and direction. Performing complex linear transformations on all frequencies is computationally expensive, so FNO truncates high-frequency components across all spatial dimensions. Given the spatial resolution $s_1 \times \dots \times s_d$ and truncation frequencies $k_{\max,j}$, $j = 1, \dots, d$, the set of preserved modes after truncation is denoted as:

$$\mathbb{Z}_{k_{\max}} = \{(k_1, \dots, k_d) \in \mathbb{Z}^{s_1} \times \dots \times \mathbb{Z}^{s_d} \mid k_j \leq k_{\max,j} \text{ or } s_j - k_j \leq k_{\max,j}, \text{ for } j = 1, \dots, d\}. \quad (7)$$

After truncation, the total number of complex parameters defined in \mathcal{R}_θ is proportional to $k_{\max,1} \times \dots \times k_{\max,d} \times d_v \times d_v$. For PDE data of lower complexity, FNO can still perform well after truncating high frequencies due to the Fourier transform’s efficient compression property. In data sampled from continuous space or time, such as natural images [61] and turbulent flows [40], the majority of the energy is concentrated in lower frequencies.

2.4 Localized Fourier Neural Operator

In this work, we propose the Localized Fourier Neural Operator to address three key challenges in applying FNO to multivariable 3D urban microclimate prediction: blurry output quality, extensive GPU memory usage, and substantial data demands. Local-FNO has three major design components: a local training strategy, geometry encoding, and patch overlapping. The local training strategy addresses all three main limitations, while geometry encoding and patch overlapping mitigate its side effects to further enhance Local-FNO’s performance. The model architecture of Local-FNO builds upon FNO while integrating recent improvements from neural operator research, as discussed in equation 5.

As shown in Figure 2, Local-FNO predicts future microclimate within each local patch. In a 3D

computational domain, patches are divided along two horizontal axes only, as microclimate complexity is typically lower along the vertical axis than the horizontal axes. The patches are divided in a uniform grid structure, aligned across both horizontal axes, with neighboring patches overlapping to share boundary areas. The total number of patches and the overlap rate can be adjusted for specific tasks. Figure 2 illustrates an example with $8 \times 8 = 64$ patches and a 20% overlap, which we apply in our prediction task.

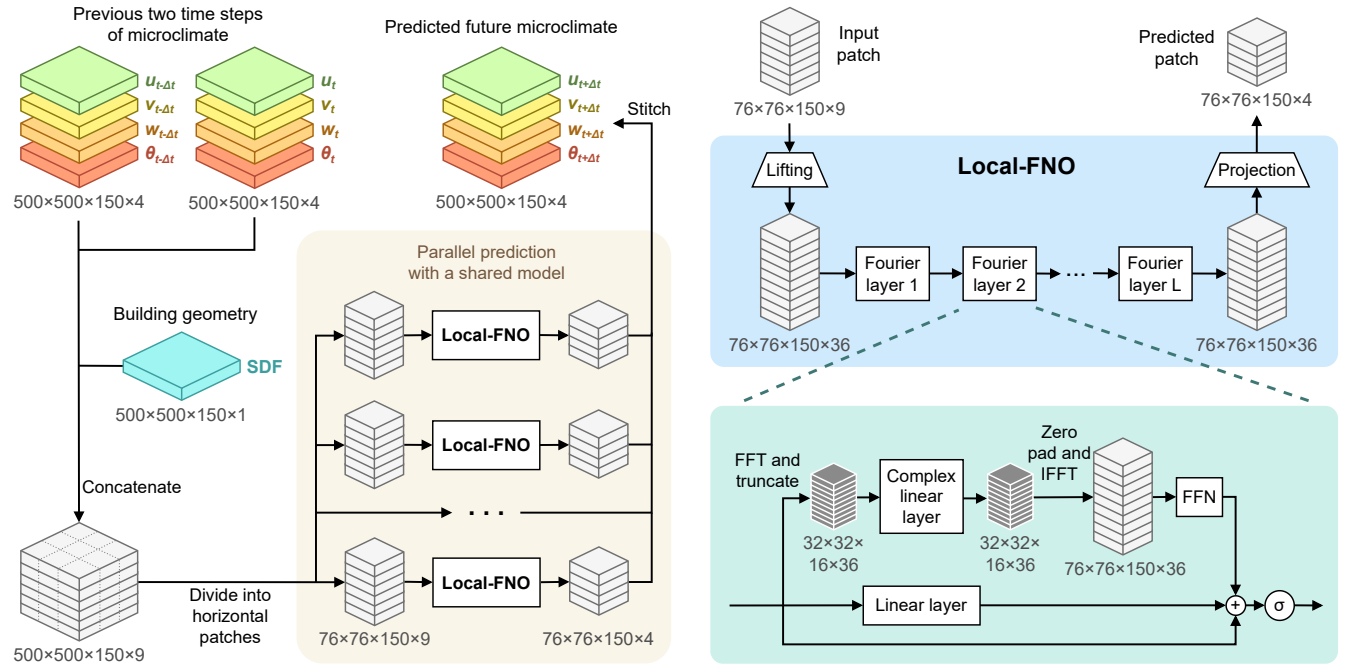


Figure 2. Overview of Local-FNO design. Left: prediction procedure of Local-FNO. Right: the architecture of Local-FNO and its Fourier layers.

Local-FNO is designed to predict urban microclimate variables at a future time step $t + \Delta t_{\text{pred}}$, based on data from two prior time steps, $t - \Delta t_{\text{pred}}$ and t , along with the signed distance function (SDF) [62] of the building geometry. Unlike in CFD, where the time step Δt is restricted by CFL conditions [63], machine learning methods do not impose such rigid criteria. As a result, the prediction interval Δt_{pred} in machine learning can be considerably larger than the time step Δt used in CFD simulations. Using two prior time intervals as inputs captures the dynamics of urban microclimate variables effectively—a strategy also employed in Graphcast [29]. Since urban microclimate is strongly influenced by local building geometry, we encode each local patch’s geometry using its SDF. This geometry encoding provides Local-FNO with the necessary building information to improve wind field predictions. Although Local-FNO is trained to predict only a single time step of microclimate ahead, it can be applied iteratively for rollout

predictions by feeding its previous prediction as input for the next step.

Patch overlapping is an essential design for Local-FNO to ensure smoother transitions between patches. Simply predicting each patch independently can cause severe discontinuity between them for two main reasons. First, each patch lacks information about the wind flow in neighboring patches, preventing continuous movement across patch boundaries. Second, FNO is designed for cyclical boundary conditions since it operates in the Fourier space. When actual boundaries are not cyclical, FNO’s prediction errors are often more pronounced near patch boundaries. Figure 3 illustrates how the patch overlapping approach is used to address these issues. Each input patch partially overlaps with its neighboring patches. First, Local-FNO takes each input patch, including its overlapping areas, to predict the corresponding output patch. In the output, overlapping regions are split evenly between neighboring patches, meaning that each patch’s boundary area is predicted by neighboring patches. This design enables information exchange between patches and avoids using Local-FNO’s own boundary predictions, which tend to have higher errors. The final output of each patch is then used iteratively for rollout predictions.

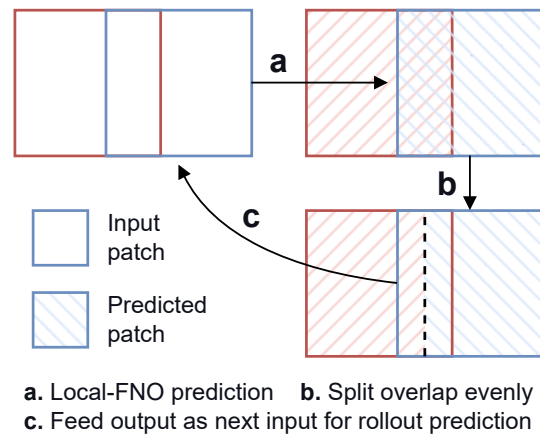


Figure 3. Patch overlapping in Local-FNO. Patch overlapping enables information exchange between patches and avoids using Local-FNO’s own boundary predictions.

By training and predicting in smaller patches, Local-FNO effectively addresses three key limitations of FNO. First, Local-FNO produces much sharper and more accurate predictions than FNO. This improvement arises because, with the same number of Fourier modes, a smaller domain size generates shorter Fourier wavelengths. For instance, in a one-dimensional domain of 1000 m, the first four Fourier wavelengths are 1000 m, 500 m, 333.3 m, and 250 m. When applied to a 100 m domain, these wavelengths shorten to 100 m, 50 m, 33.3 m, and 25 m. In FNO, shorter wavelengths allow for better capture

of small-scale features in the urban wind field. Secondly, Local-FNO breaks down the full-domain microclimate prediction into smaller, independent tasks, greatly lowering memory demands. This design also supports scalability for large-scale microclimate predictions, as the workload can be distributed across multiple GPUs. Third, Local-FNO improves generalization and requires less data to make accurate predictions. By focusing on local features, it learns from smaller, more relevant wind patterns, reducing the risk of capturing spurious global correlations in data-limited scenarios. Dividing data into smaller patches also increases data efficiency, as it reduces dimensionality and expands the number of training samples without requiring extra raw data.

2.5 Model training

For each time step, the CityFFD simulation has a total grid size of $600 \times 600 \times 150$ along the x , y , and z axes, covering a physical area of $4 \text{ km} \times 4 \text{ km} \times 1 \text{ km}$. The central area of interest has a grid size of $500 \times 500 \times 150$, corresponding to a physical area of $2 \text{ km} \times 2 \text{ km} \times 1 \text{ km}$. Only data from this area of interest is used for machine learning. We conduct a CityFFD simulation for a total of 23000 steps, with a time step Δt of 0.2 s. The flow field reaches full development around 8000 steps. For the remaining 15000 steps, we save data at every 10th step, resulting in 1500 saved time steps that represent 50 minutes of wind field data. Each time step contains three directional wind speeds, u , v , and w , and temperature θ . We sequentially split the 50-minute dataset into 44 minutes for training, 3 minutes for validation, and 3 minutes for testing. The training set is used to train both the FNO and Local-FNO models, while the validation set is reserved for hyperparameter tuning and early stopping. The test set is solely used to evaluate model performance, remaining fully inaccessible during training.

Our goal is to use machine learning models to predict multivariable 3D urban microclimate across full grids of $500 \times 500 \times 150$. However, training models directly on these full grids would require extensive computational resources that exceed our device capabilities. To make training feasible, we utilize FNO's resolution-invariant property: FNO trained on downsampled data can be applied directly to predict at the original resolution. Therefore, we downsample the full grid data from $500 \times 500 \times 150$ to a half-resolution grid of $250 \times 250 \times 75$ for training. FNO trains on the entire domain, while Local-FNO further divides the domain into smaller patches for training.

We train both FNO and Local-FNO using root mean square error (RMSE) loss. Let \hat{u} , \hat{v} , \hat{w} , and $\hat{\theta}$ be the predicted variables, and u , v , w , and θ be the ground truth. Let s_x , s_y , and s_z represent the spatial resolution of the sample along the x , y , and z axes, respectively, and let N_{batch} denote the number of samples per batch. The RMSE loss is given by:

$$\text{loss}_{\text{RMSE}} = \sqrt{\frac{\sum_{n,x,y,z} ((\hat{u}_{n,x,y,z} - u_{n,x,y,z})^2 + (\hat{v}_{n,x,y,z} - v_{n,x,y,z})^2 + (\hat{w}_{n,x,y,z} - w_{n,x,y,z})^2 + (\hat{\theta}_{n,x,y,z} - \theta_{n,x,y,z})^2)}{N_{\text{batch}}s_x s_y s_z}} \quad (8)$$

To ensure a fair comparison, both FNO and Local-FNO models with varying patch numbers use the same model architecture: 4 layers, a hidden dimension of 36, and truncation modes of 16, 16, and 8 for the x , y , and z axes, respectively. This setup allows vanilla FNO to train on half-resolution grid data using a 32 GB GPU with a batch size of 1. The training hyperparameters are consistent across models, with a learning rate of 2.0×10^{-3} , a step scheduler reducing the learning rate by 0.5 per epoch, and the Adam optimizer with a weight decay of 1.0×10^{-4} . The only differing hyperparameter between FNO and Local-FNO is the batch size. Smaller patches require less memory, so we assign a larger batch size to models with smaller patches to fully utilize the 32 GB of GPU memory. The batch sizes for each model are shown in Table 1. 8×8 denotes that the entire domain is divided into 64 local patches. All Local-FNO models use the same overlap rate of 20%. With patch overlapping, some wind field grid data points are computed multiple times within a single epoch, which increases the training time. A 20% overlap rate can result in approximately $120\% \times 120\% = 144\%$ of the training time per epoch compared to training without overlap. For the implemented models, the training time per epoch is 0.40 hours for FNO and Local-FNO without patch overlapping, and 0.62 hours for Local-FNO with 20% patch overlapping.

Model	Training patch size	Batch size	Epochs at stop	Learning rate at stop
FNO	$250 \times 250 \times 75$	1	4	2.5×10^{-4}
Local-FNO (2×2)	$139 \times 139 \times 75$	3	6	6.3×10^{-5}
Local-FNO (4×4)	$74 \times 74 \times 75$	10	7	3.1×10^{-5}
Local-FNO (8×8)	$38 \times 38 \times 75$	42	9	7.8×10^{-6}

Table 1. Training specifics for FNO and Local-FNOs with 20% of patch overlapping and varying patch numbers. The prediction interval is 20 s. All models consume nearly the same amount of GPU memory.

To prevent overfitting, particularly as vanilla FNO tends to overfit on the entire domain, we employ an early stopping technique. Validation loss is monitored each epoch, and training is stopped if the validation loss starts increasing. The model with the lowest validation loss is retained. The maximum number of epochs is set to 12. Table 1 reports the epochs at stop and learning rates at stop for FNO and Local-FNOs with different patch numbers at a 20 s prediction interval. Results show that with increased patch numbers and smaller patch sizes, Local-FNO can be trained for more epochs at a lower learning rate without overfitting. The prediction interval also influences the stopping epochs for all models: with shorter intervals, where flow field changes are minimal, the model learns more effectively and tends to overfit less. Conversely, larger intervals with greater flow changes make the model more prone to overfitting.

3 Results and discussion

In this section, we evaluate the performance of Local-FNO in predicting multivariable 3D urban microclimate. We begin with an integral time scale analysis to highlight the rapid temporal changes in the flow field. Next, we evaluate Local-FNO’s rollout prediction performance, examining both the predicted instantaneous flow fields and statistical flow characteristics. Finally, we demonstrate the performance improvement of Local-FNO compared upon FNO.

3.1 Integral time scale analysis of the flow field

Turbulent systems at different scales exhibit varying levels of complexity. To gain a clearer understanding of the temporal dynamics of the urban microclimate simulation data, we perform an integral time scale analysis. The integral time scale represents the timespan over which fluctuations in turbulent flow remain correlated [64]. A shorter integral time scale means that turbulent structures lose correlation more quickly, suggesting a more chaotic or rapidly changing flow.

To compute the integral time scale for the u component of the wind speed time series $u_{t(i)}$, $i = 1, \dots, N$ at a specific location, we first calculate its temporal autocorrelation $R_u(\tau)$ at each time lag τ :

$$R_u(\tau) = \frac{\sum_{i=1}^{N-\tau} (u_{t(i)} - \bar{u}) (u_{t(i+\tau)} - \bar{u})}{\sum_{i=1}^{N-\tau} (u_{t(i)} - \bar{u})^2}, \quad (9)$$

where $\bar{u} = \frac{1}{N} \sum_{i=1}^N u_{t(i)}$ is the time averaged u velocity. We then find the time lag at the first zero crossing, τ_{\max} . The integral time scale for the u component is defined as the area under the autocorrelation curve up to τ_{\max} :

$$\mathcal{T}_u = \sum_{\tau=0}^{\tau_{\max}} R_u(\tau) \Delta t . \quad (10)$$

The final integral time scale is reported as an average of the u , v , and w components:

$$\bar{\mathcal{T}} = \frac{\mathcal{T}_u + \mathcal{T}_v + \mathcal{T}_w}{3} . \quad (11)$$

We compute the integral time scale across all locations within in a $1.5 \text{ km} \times 1.5 \text{ km} \times 100 \text{ m}$ domain with compact building distribution for 10 minutes of period and present the statistics in Figure 4.

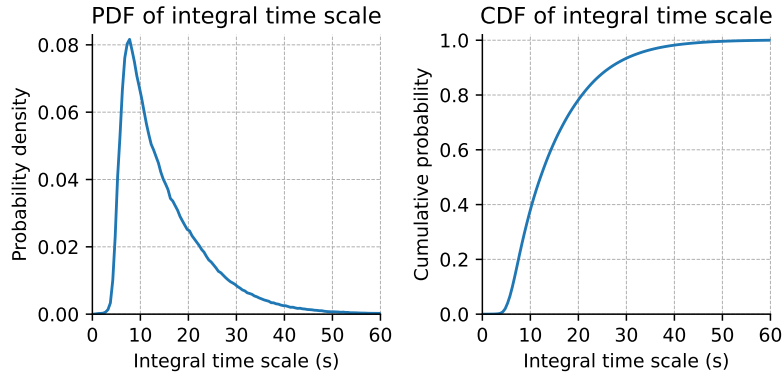


Figure 4. Probability density function (PDF) and cumulative distribution function (CDF) of the integral time scale in the central $1.5 \text{ km} \times 1.5 \text{ km} \times 100 \text{ m}$ domain with compact building distribution.

Figure 4 shows that approximately 50% of locations have an integral time scale under 12 s, and around 80% have an integral time scale under 20 s. The PDF peaks at 8 s, indicating the most frequent time scale. The average integral time scale is 14.9 s, indicating that velocity fluctuations in the flow field lose correlation roughly every 15 s, making accurate turbulence prediction a challenging task.

3.2 Evaluation of prediction performance of Local-FNO

In this section, we assess the prediction performance of Local-FNO on full grid microclimate data ($500 \times 500 \times 150$) with three directional velocity components u , v , w , and the temperature θ .

3.2.1 Rollout prediction performance

Unlike CFD, where CFL conditions restrict time steps [63], machine learning methods allow greater flexibility in setting the prediction interval. Shorter prediction intervals improve immediate accuracy but accumulate more errors over time. Conversely, larger prediction intervals reduce the frequency of error accumulation but may miss rapid weather changes, leading to blurrier results. Figure 5 illustrates the impact of prediction interval length on Local-FNO's performance. Local-FNO is configured with 8×8 patches and a 20% overlap, as this setup yields relatively optimal performance (see section 3.3 for details).

We use two metrics to evaluate prediction performance: RMSE and fluctuation correlation. RMSE measures the average error magnitude between predicted results and simulation data, with lower values indicating that predictions are generally closer to observed values. The RMSE for a variable u is defined as

$$\text{RMSE}_u = \sqrt{\frac{1}{s_x s_y s_z} \sum_{x,y,z} (\hat{u}_{x,y,z} - u_{x,y,z})^2}, \quad (12)$$

where \hat{u} and u represent the prediction and ground truth, respectively, and s_x , s_y , and s_z are the spatial resolutions along the x , y , and z axes. The computation is similar for other variables. RMSE alone, however, only captures the average error magnitude and does not reflect changes in turbulence patterns over space and time. To evaluate how well the prediction captures wind field fluctuations, we also report the fluctuation correlation. The fluctuation correlation $R_{\text{fluc},u}$ for a variable u is computed as

$$R_{\text{fluc},u} = \frac{\sum_{x,y,z} (\hat{u}_{x,y,z} - \bar{u}_{x,y,z})(u_{x,y,z} - \bar{u}_{x,y,z})}{\sqrt{\sum_{x,y,z} (\hat{u}_{x,y,z} - \bar{u}_{x,y,z})^2} \sqrt{\sum_{x,y,z} (u_{x,y,z} - \bar{u}_{x,y,z})^2}}, \quad (13)$$

where \bar{u} is the steady-state time-averaged value of u for the simulation data. \bar{u} remains stable after the wind field has developed. A higher fluctuation correlation indicates that the prediction accurately represents the spatial and temporal dynamics of the wind field. A model that only captures time-averaged flow may still have a low RMSE but will show a fluctuation correlation close to 0. In weather forecasting, fluctuation correlation is often referred to as the anomaly correlation coefficient (ACC) and is commonly

used to evaluate the prediction performance [28, 30].

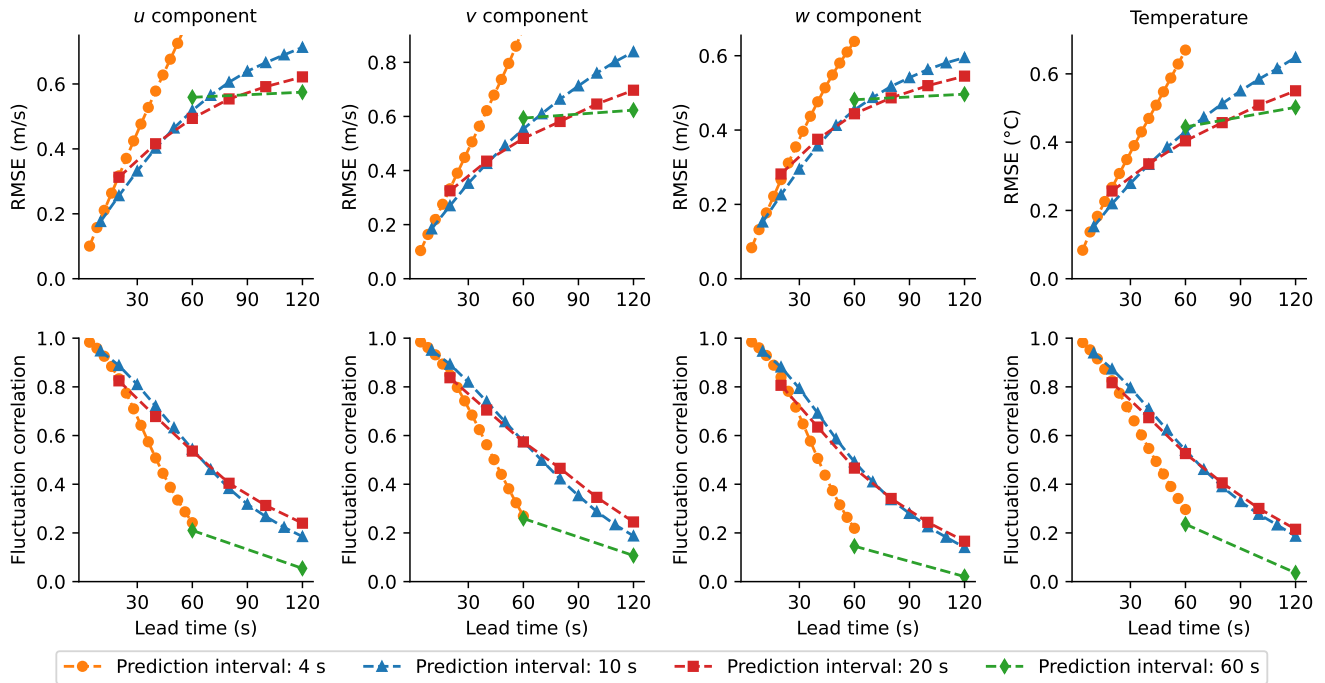


Figure 5. Rollout prediction performance of Local-FNOs with varying prediction intervals.

As shown in Figure 5, RMSE values increase with longer lead times for all variables, indicating that prediction error grows over time. Fluctuation correlation values also decrease for all variables as lead time extends, reflecting a decline in accuracy for capturing turbulence patterns. A shorter prediction interval, such as 4 s, has the lowest initial RMSE but accumulates errors quickly. A longer interval, like 60 s, shows slower RMSE growth but suffers from low fluctuation correlation, missing rapid spatial and temporal fluctuations patterns. Moderate intervals like 10 and 20 s provide the best overall performance: for the first 60 s, a 10 s interval achieves the lowest RMSE and highest fluctuation correlation, while after 60 s, a 20 s interval gives the most satisfactory results. These intervals, 10 and 20 s, are 50 and 100 times longer than the CFD time step of 0.2 s, demonstrating that machine learning methods can operate effectively with a much longer prediction interval than CFD simulations. This advantage is a key reason why machine learning methods can be more efficient than CFD solvers in simulating turbulence.

In Table 2, we present the prediction performance of Local-FNO with its best-performing prediction interval. For the prediction period from 0 to 60 s, RMSE values for the three directional wind speeds and temperature remain low (e.g., 0.380 m/s for the v component and 0.300 °C for temperature). Fluctuation

Prediction period	Metric (time-averaged)	u component	v component	w component	Temperature
0-60 s	RMSE	0.358 m/s	0.380 m/s	0.316 m/s	0.300 °C
	Fluctuation correlation	0.757	0.772	0.732	0.747
0-120 s	RMSE	0.498 m/s	0.534 m/s	0.442 m/s	0.419 °C
	Fluctuation correlation	0.499	0.529	0.443	0.490

Table 2. Time-averaged rollout prediction performance of Local-FNO using the best-performing prediction intervals.

correlations are high, with values above 0.732 for all components, indicating that Local-FNO effectively captures dynamic fluctuation patterns in the wind field. As discussed in Section 3.1, the average integral time scale of the wind field is 14.9 s. Thus, a 60 s prediction period—four times the integral time scale—demonstrates that Local-FNO can provide accurate predictions even after substantial changes in the flow field. Even as the prediction period increases to 120 s, the RMSE values remain relatively low (e.g., 0.534 m/s for the v component and 0.419 °C for temperature).

3.2.2 Visualization of instantaneous flow field

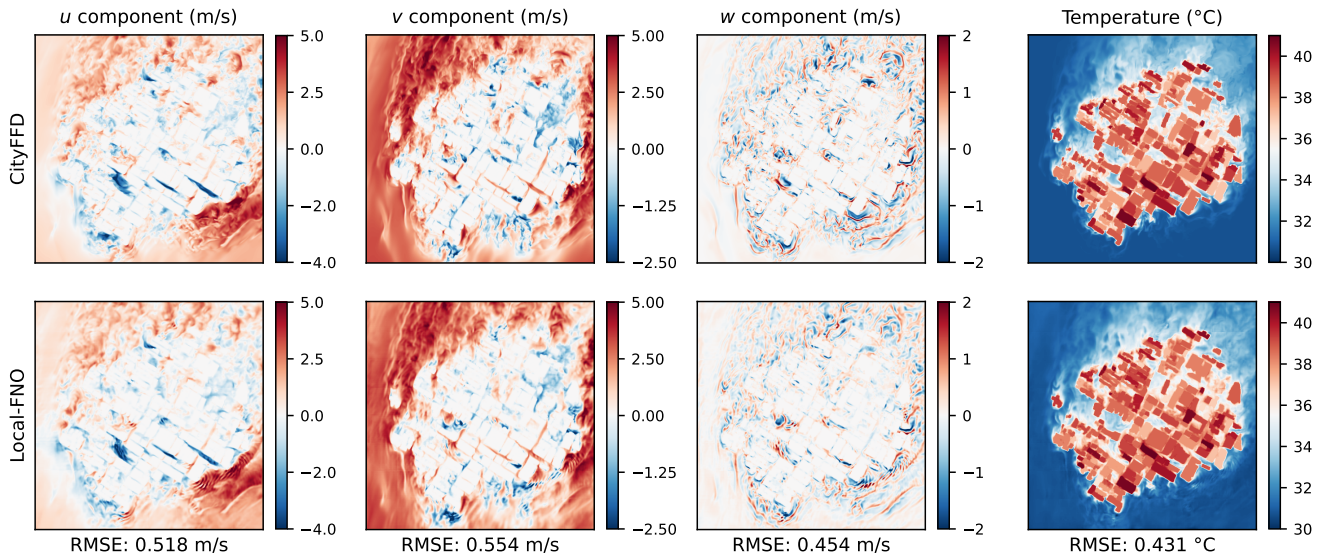


Figure 6. Instantaneous flow field from simulation and Local-FNO prediction, visualized on the $z = 10$ m horizontal plane at 60 s.

Figure 6 and Figure 7 present instantaneous visualizations of the velocity components u , v , w , and the temperature θ from both CityFFD simulation and Local-FNO prediction at a lead time of 60 s, shown in the horizontal and vertical planes, respectively. In the first three columns of the velocity fields, CityFFD results highlight pronounced high-speed zones around buildings, along with vortex shedding in

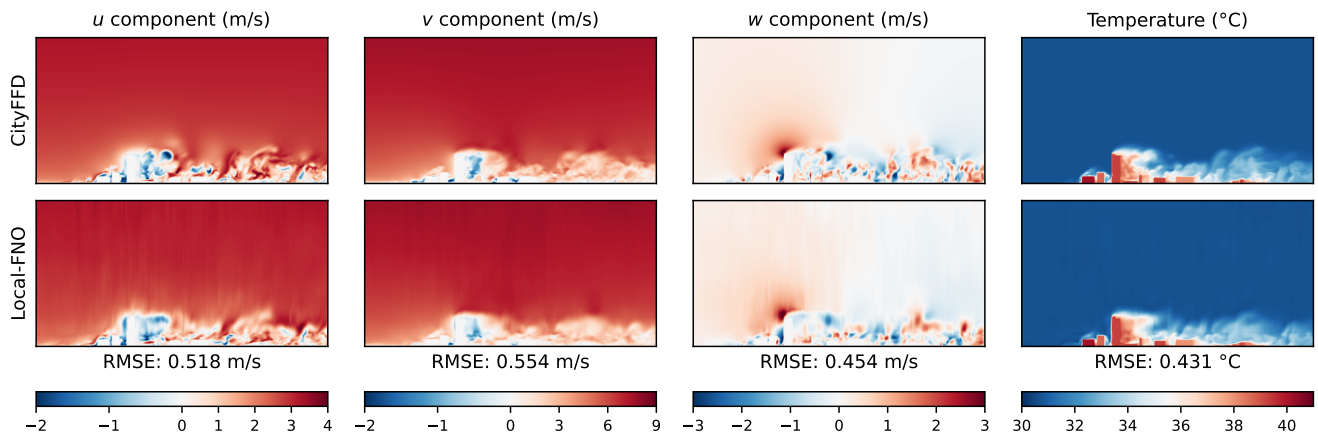


Figure 7. Instantaneous flow field from simulation and Local-FNO prediction, visualized on the vertical plane along the y -axis intersecting the tallest building at 60 s.

their wake. In dense urban environments, airflow passes through narrow gaps and open channels between buildings, creating alternating regions of acceleration and deceleration. Flow separation at building edges downstream generates eddies, inducing vortices that subsequently detach from the structures and create meandering flow patterns in wake regions (see the first two columns in Figure 6). These vortices interact with building roofs, contributing to complex recirculation zones and the formation of mixing layers within the urban canopy layer (see Figure 7). Local-FNO effectively captures primary structural characteristics of urban airflow, such as flow separation, vortex shedding, and turbulent wake effects within urban building environments, achieving RMSE values of 0.518 m/s, 0.554 m/s, and 0.454 m/s across the three directional velocity components. However, minor discrepancies in velocity magnitude remain in highly turbulent regions.

In the temperature field, hotter regions in the CityFFD simulation results are primarily located within dense building areas (see Figure 6). In these zones, stable airflow restricts the mixing of warm and cool air, causing heat to build up. Additionally, the close proximity of buildings reduces natural ventilation, further restricting heat dispersion (see Figure 7). In contrast, cooler areas appear in open spaces and along wider pathways, where freer airflow allows for more efficient heat dissipation. The Local FNO model accurately captures these temperature patterns, including thermal gradients and heat build-up around buildings, achieving an RMSE of 0.431 °C. Minor discrepancies arise near building edges and wake regions, where complex temperature dynamics arise due to flow separation and vortex shedding.

3.2.3 Visualization of statistical characteristics of flow field

In addition to the instantaneous flow fields, we further examine the statistical characteristics of Local-FNO predictions over a time period. Figure 8 presents horizontal slices of the mean velocity magnitude, turbulent kinetic energy, mean temperature, and temperature variance from both CityFFD simulations and Local-FNO predictions over the 0-120 s period, with a 50 m height selected to highlight complex urban turbulent flow.

Given N discrete time steps, the mean velocity magnitude for a specific location is computed as:

$$|\overline{U}| = \frac{1}{N} \sum_{i=1}^N \sqrt{u_{t(i)}^2 + v_{t(i)}^2 + w_{t(i)}^2}. \quad (14)$$

The turbulent kinetic energy (TKE) is defined as:

$$\text{TKE} = \frac{1}{2} \frac{1}{N} \sum_{i=1}^N \left((u_{t(i)} - \bar{u})^2 + (v_{t(i)} - \bar{v})^2 + (w_{t(i)} - \bar{w})^2 \right), \quad (15)$$

where $\bar{u} = \frac{1}{N} \sum_{i=1}^N u_{t(i)}$, and similarly for \bar{v} and \bar{w} .

The mean temperature is given by $\bar{\theta} = \frac{1}{N} \sum_{i=1}^N \theta_{t(i)}$, and the temperature variance is computed as:

$$\sigma_{\theta}^2 = \frac{1}{N} \sum_{i=1}^N (\theta_{t(i)} - \bar{\theta})^2. \quad (16)$$

In the CityFFD results, high-velocity zones were observed within narrow gaps and along building edges, accompanied by high turbulence intensity (first two columns). These rapid directional changes create shear layers, where differences in velocity induce instability. This instability further causes the rolling and rotation of eddies, which promotes turbulence generation and increases TKE in the flow field. In terms of temperature, the mean temperature plot (third column) shows elevated temperatures concentrated around areas with dense buildings, where restricted airflow leads to thermal buildup. The temperature variance plot (fourth column) highlights areas with variable thermal conditions, indicating strong temperature mixing. Higher temperature variance is apparent near building edges and in wake regions behind buildings, where turbulence enhances convective mixing and causes intermittent interactions between cooler air and warmer surfaces.

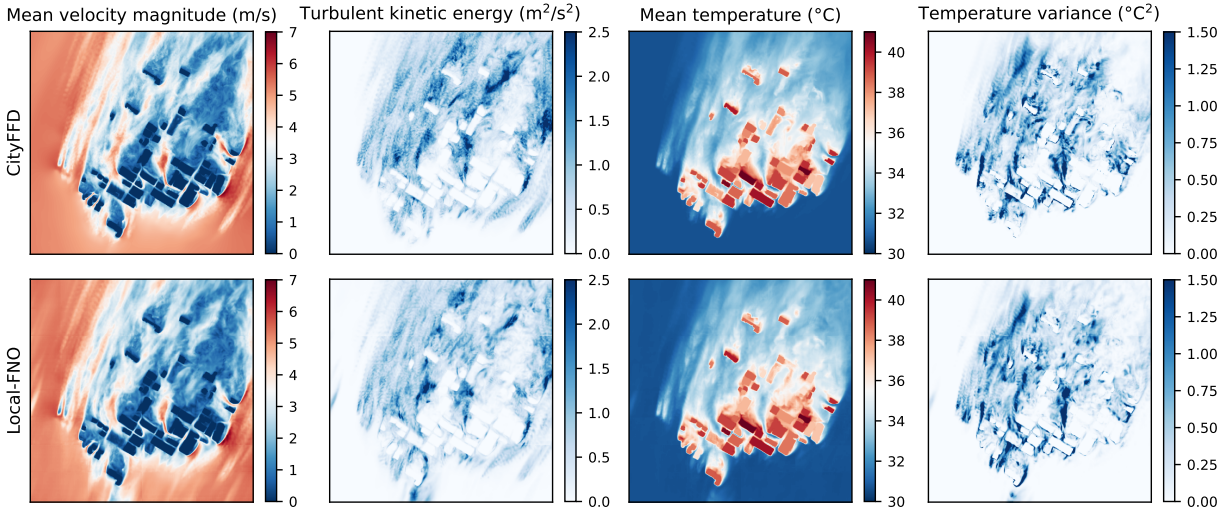


Figure 8. First and second-order flow field statistics from simulation and Local-FNO prediction, visualized on the $z = 50$ m horizontal plane over the 0-120 s period.

Local-FNO's predictions are highly consistent with CityFFD for first-order statistical characteristics, such as mean velocity magnitude and mean temperature. Local-FNO effectively captures steady-state spatial patterns of both velocity and temperature. For velocity, Local-FNO replicates high-velocity regions formed by street canyons and low-velocity regions due to building drag effects, similar to CityFFD. For temperature, it accurately captures warmer zones near buildings and the temperature gradients between buildings and open spaces. For second-order characteristics, such as TKE and temperature variance, Local-FNO generally aligns well with CityFFD, particularly around building edges and within street canyons where fluctuations are largest. However, at certain highly turbulent locations, Local-FNO shows slight intensity differences. This is likely due to the complex high-frequency interactions that these second-order statistics represent, which are challenging to capture precisely. Overall, Local-FNO achieves notable accuracy in replicating CityFFD's airflow and thermal distributions, underscoring its reliability in modeling complex urban wind dynamics.

We further analyze the statistical coupling between velocity and temperature. Figure 9 illustrates the turbulent heat flux components (u , v , and w) for both the CityFFD (top row) and Local-FNO (bottom row), with each column corresponding to a different directional heat flux component. For example, the heat flux in the x direction represents the average correlation between temperature fluctuations and u

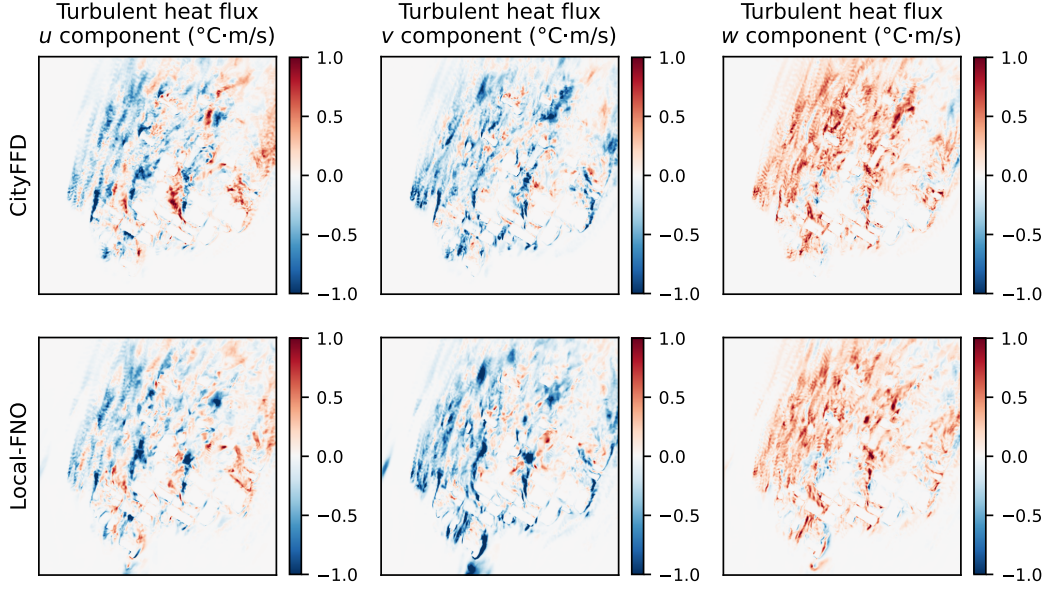


Figure 9. Turbulent heat flux in three directions from simulation and Local-FNO prediction, visualized on the $z = 50$ m horizontal plane over the 0-120 s period.

fluctuations, defined as:

$$q_x = \frac{1}{N} \sum_{i=1}^N (u_{t(i)} - \bar{u}) (\theta_{t(i)} - \bar{\theta}) . \quad (17)$$

where \bar{u} and $\bar{\theta}$ are time-averaged u velocity and temperature.

For the u and v components of turbulent heat flux, the alternating red-blue distribution represents dynamic, significant heat transfer influenced by turbulent eddies in densely built areas. Positive zones (red) indicate heat moving along the positive axis direction, while negative zones (blue) indicate cooler air flowing along the positive axis direction. This pattern of alternating colors reflects fluctuating temperature gradients, where intense turbulence drives rapid shifts in heat movement from warmer to cooler regions. Such alternating regions are a direct result of turbulent mixing, particularly prominent in high-density building areas due to vortex shedding and recirculation zones [65]. As the primary wind direction aligns more closely with the y -axis (v component), crosswind effects around buildings have a stronger impact on the u component, especially around narrow streets and building edges, where lateral turbulence enhances heat transfer. In the w component, which represents vertical heat flux between the surface and the atmosphere, the plots show predominantly red regions, indicating strong upward heat transfer. These

red zones reflect areas where heat moves vertically, facilitating thermal energy exchange between the surface and atmosphere. This upward flux is particularly prominent in wake regions and above structures, where building-induced turbulence and surface heating cause warm air to rise.

For all directions, Local-FNO produces a comparable pattern of red and blue regions, indicating that it captures the primary direction and magnitude of heat transport driven by turbulence. Some finer details appear slightly smoothed, particularly near building edges and within narrow streets where sharp flux changes are expected. In general, Local-FNO provides a strong representation of heat exchange processes in urban microclimate with temperature variations. Accurate prediction of this complex heat flux pattern is vital in urban environments as it impacts both local thermal comfort and larger-scale phenomena like urban heat islands.

3.2.4 Improvement from patch overlapping

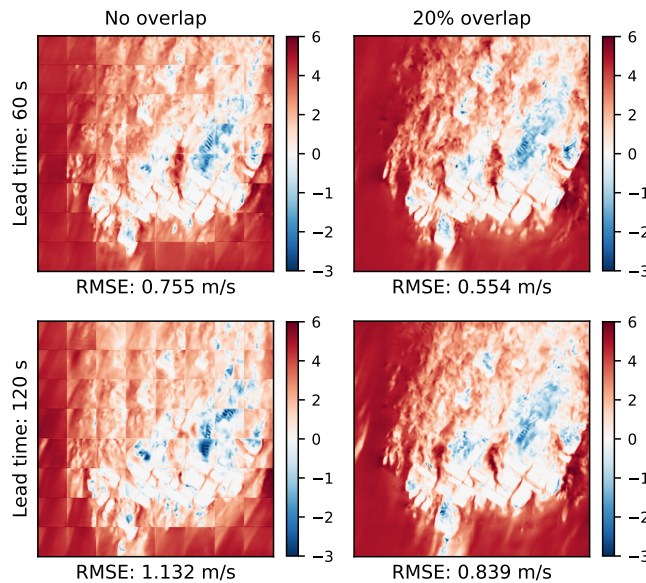


Figure 10. Instantaneous predictions of the v component from Local-FNOs without and with patch overlapping, visualized on the $z = 50$ m horizontal plane at 60 s and 120 s.

Patch overlapping is a key component in Local-FNO to ensure smoother transitions between patches. Figure 10 shows a comparison of Local-FNO (8×8) predictions without and with patch overlapping. Without overlap, Local-FNO’s prediction exhibits grid artifacts in blocky patterns, which become more pronounced as the prediction lead time increases from 60 s to 120 s. These artifacts arise because the air in the actual flow field continuously interacts across neighboring regions, transferring both kinetic

energy and heat. As lead time increases, Local-FNO's independent local predictions without overlap make patches drift further from the actual flow field. In contrast, with a 20% overlap, grid artifacts are significantly reduced, creating smoother transitions across patches and a more coherent spatial structure. Even at a lead time of 120 s, Local-FNO with overlapping patches exhibits minimal grid artifacts, demonstrating that patch overlapping effectively facilitates flow interactions across neighboring patches and mitigates the side effects of independent local predictions.

3.2.5 Computational efficiency

CityFFD and Local-FNO both leverage GPU acceleration. CityFFD requires 4.6 s to compute per time step, whereas Local-FNO takes 9.8 s for a full grid ($500 \times 500 \times 150$) prediction. Therefore, the speedup of Local-FNO depends mainly on its prediction interval. With a CFD time step of 0.2 s and a 20 s prediction interval, Local-FNO achieves a 47 times speedup on full grid microclimate data. As Local-FNO is resolution-invariant, further acceleration can be achieved by predicting on half-resolution grid ($250 \times 250 \times 75$). This further reduces the computation time for prediction to 0.95 s and results in a 480 times speedup.

3.3 Prediction performance improvements of Local-FNO over FNO

This section presents the performance improvements achieved by Local-FNO over the vanilla FNO model. Due to GPU memory constraints, predicting on the full grid microclimate data ($500 \times 500 \times 150$) with vanilla FNO exceeds our device's capacity. Therefore, all models in this section predict on half-resolution grid ($250 \times 250 \times 75$) to ensure a fair comparison.

3.3.1 Improvement in rollout prediction performance

Figure 11 shows the rollout prediction performance comparison between FNO and Local-FNOs with different patch numbers. In this context, 8×8 denotes that the entire domain is divided into 64 local patches. FNO can be treated as a special case of Local-FNO with a single patch. As illustrated in Figure 11, Local-FNOs outperform FNO across all metrics and lead times, exhibiting lower RMSE and higher fluctuation correlation. Performance improvements are particularly notable when increasing from 1 to 2×2 patches and from 2×2 to 4×4 patches. However, improvements are limited from 4×4 to 8×8 patches. This diminishing return trend suggests that increasing the number of patches beyond a certain

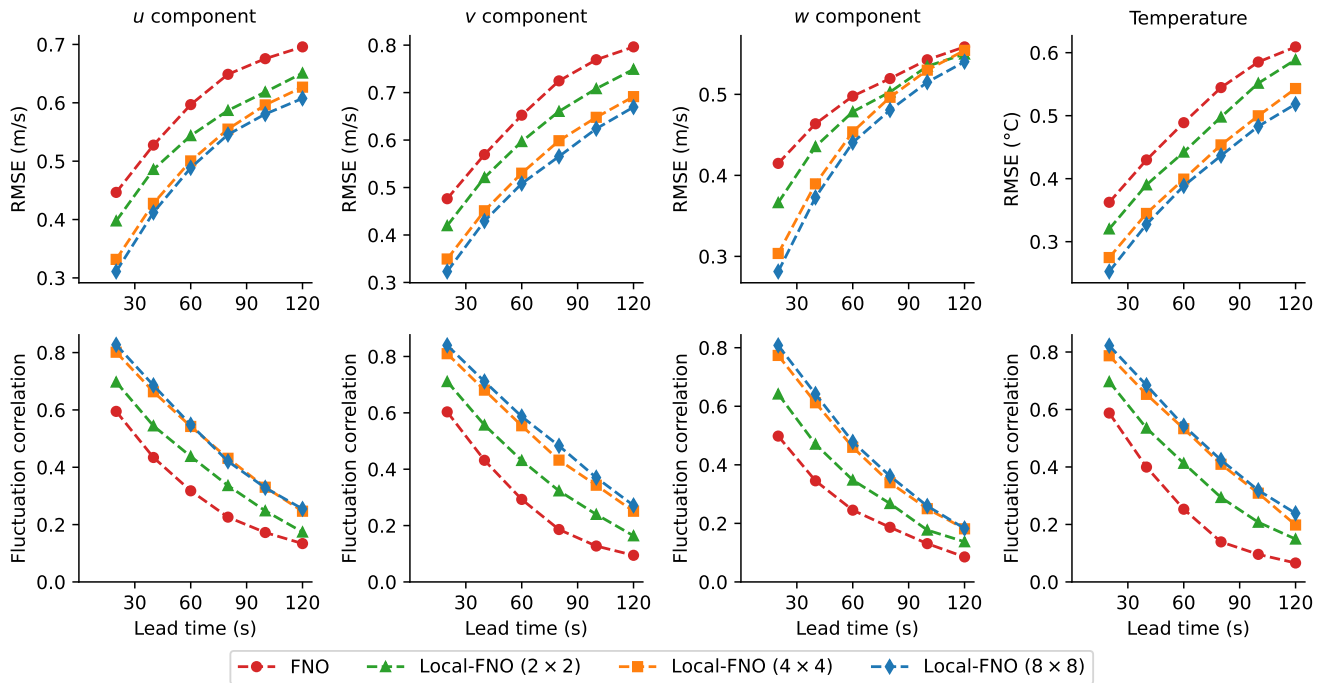


Figure 11. Rollout prediction performance of FNO and Local-FNOs with varying patch numbers.

point yields smaller benefits, with 8×8 patches providing the best overall performance. During the 0-60 s period, Local-FNO (8×8) shows a significant improvement over FNO in prediction performance, reducing RMSE by 23.5%, 26.3%, 21.1%, and 24.9% for the u , v , w , and θ components, respectively, reflecting a lower average error magnitude. Additionally, Local-FNO (8×8) achieves fluctuation correlations that are 45.2%, 50.1%, 46.0%, and 47.7% closer to 1 for the u , v , w , and θ components, reflecting greater accuracy in capturing turbulence pattern fluctuations over space and time.

3.3.2 Improvement in instantaneous flow field

Figures 12 and 13 display the instantaneous velocity component v and temperature θ at a 60 s lead time, comparing predictions from FNO and Local-FNOs with different patch numbers. Within 60 s, small-scale turbulence patterns change significantly. Compared to the CityFFD simulation, FNO's predictions appear blurry and fail to capture the small-scale turbulence in both velocity and temperature. As discussed in Section 2.4, this limitation arises because FNO preserves only a limited number of low-frequency Fourier modes. Fourier modes defined on larger domains have longer wavelengths, which are ineffective for representing small-scale features. Additionally, FNO's direct training on whole-domain, high-dimensional data makes it prone to overfitting, especially with limited training samples. Prior research showed that

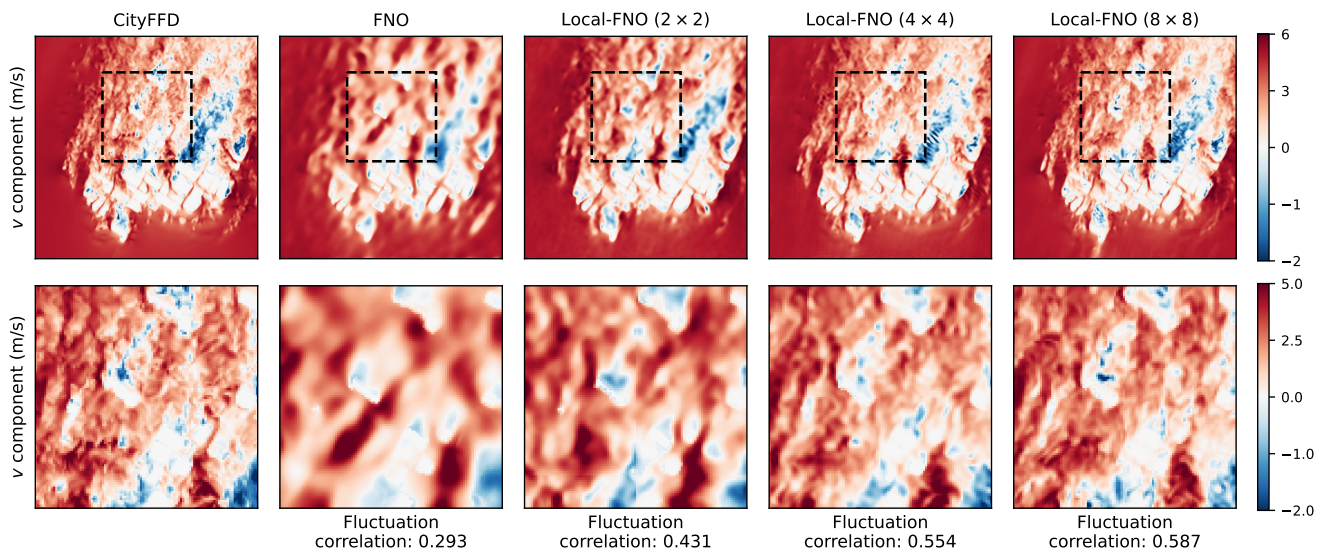


Figure 12. Instantaneous predictions of the v component from FNO and Local-FNOs with varying patch numbers, visualized on the $z = 50$ m horizontal plane at 60 s.

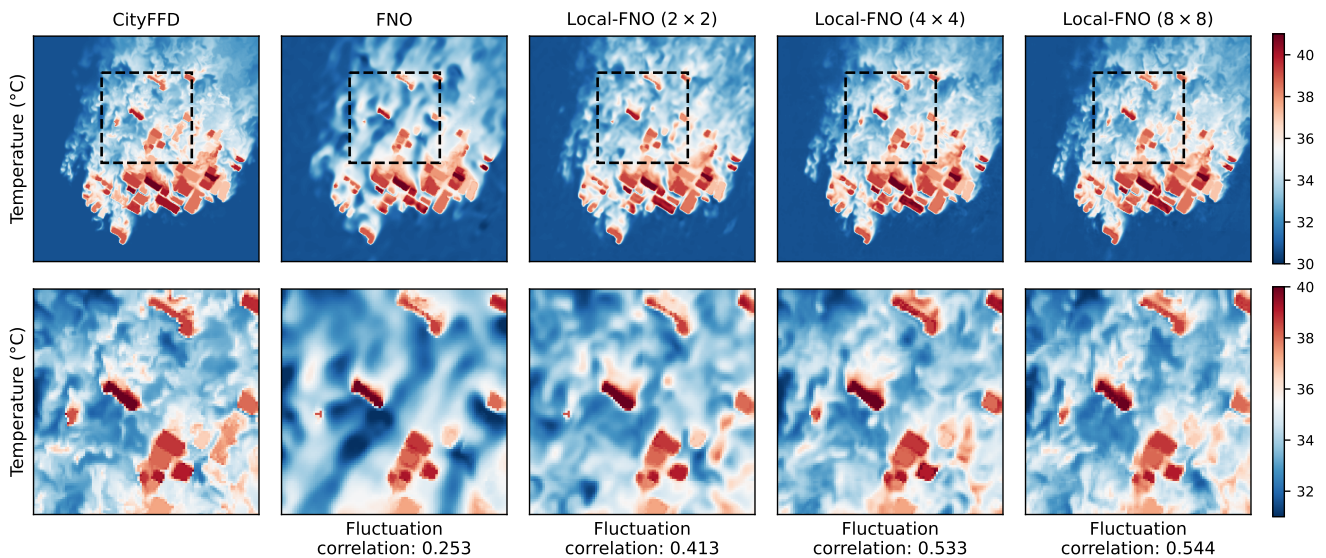


Figure 13. Instantaneous temperature predictions from FNO and Local-FNOs with varying patch numbers, visualized on the $z = 50$ m horizontal plane at 60 s.

FNO can deliver satisfactory predictions in simpler wind fields over shorter prediction intervals (0.1 s) [41]. However, as turbulence complexity and the prediction interval grow, its predictions degrade, producing a blurry flow field that no longer accurately reflects turbulence characteristics.

Compared to FNO, Local-FNOs provide significantly clearer flow fields for both velocity and temperature. As the number of patches increases, the size of each patch decreases, allowing Local-FNO to produce sharper and more accurate flow field predictions. This suggests that Fourier modes defined on smaller patches more effectively capture small-scale features in complex turbulence. For instance, Local-FNO (8×8) improves turbulent fluctuation correlation from 0.293 to 0.587 for the v component and from 0.253 to 0.544 for temperature, compared to FNO.

3.3.3 Improvement in energy spectra

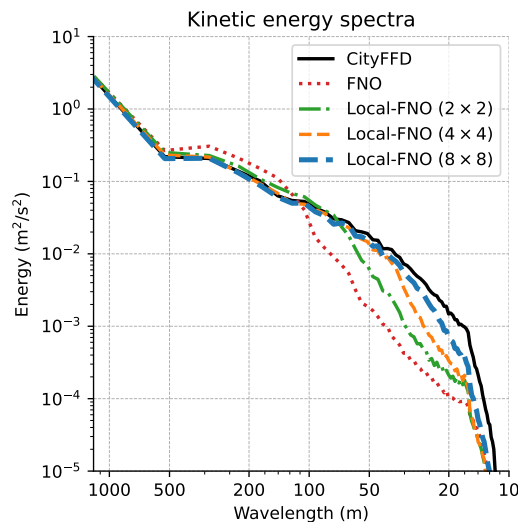


Figure 14. Kinetic energy spectra of velocity field predictions from FNO and Local-FNOs with varying patch numbers, computed on the $z = 50$ m horizontal plane at 60 s.

Energy spectra provide a quantitative measure of the blurriness in flow fields, representing how the kinetic energy of turbulence is distributed across various spatial scales [40]. It's commonly used to evaluate whether machine learning predictions can capture complex multi-scale turbulence patterns. Figure 14 shows the energy spectra for velocity field predictions from FNO and Local-FNOs with different patch numbers. In the CityFFD simulation, energy gradually declines as wavelength decreases, showing a smooth, continuous drop across scales. The FNO prediction, in comparison, overestimates energy at scales above 100 m and underestimates it at scales below 100 m, indicating a limitation in predicting

small-scale turbulence details. This limitation is also observed in other studies as the spectral bias of FNO [44, 48]. In urban environments, structures such as dense buildings and pathways can generate complex flow patterns at scales below 100 m. Accurate representation of turbulence at these scales is crucial for modeling wind interactions with urban structures. Local-FNO, with increased patch numbers and smaller patch sizes, aligns more closely with CityFFD energy spectra across all scales, with significant improvements between 100 m and 20 m. A 20 m wavelength corresponds to a 10 m resolution according to the sampling theorem [66], demonstrating the effectiveness of Local-FNO in accurately predicting complex urban wind flows.

4 Conclusions

In this study, we developed a novel Local-FNO model to achieve accurate and efficient predictions for multivariable, high-resolution 3D urban microclimate. For the rapidly changing turbulence in urban environments, Local-FNO is capable of making accurate predictions of instantaneous flow field over 60 seconds, four times the average integral time scale. Additionally, it accurately captures statistical flow characteristics, including turbulent kinetic energy and turbulent heat flux, over a 120 seconds period. This demonstrates Local-FNO's ability to model both individual variables (three directional velocities and temperature) and their correlations. Running on a single 32 GB GPU, Local-FNO can predict high-resolution urban microclimate data with 150 million ($500 \times 500 \times 150 \times 4$) feature dimensions. For the same prediction lead time, it achieves nearly 50 times the speed of a CFD solver, with an average error of 0.35 m/s for velocity and 0.30 °C for temperature over the first 60 seconds. These findings demonstrate the potential of machine learning for efficiently and accurately solving complex fluid dynamics in urban environments with temperature variations. Local-FNO is capable of capturing turbulence patterns down to a 10 m resolution within a $2 \text{ km} \times 2 \text{ km}$ domain. Although Local-FNO does not yet match the precision of numerical solvers, it offers meaningful results at much faster speeds, which can support practical applications like energy-efficient urban planning and carbon reduction. Moreover, studies suggest that with larger models and expanded training data, the accuracy of end-to-end trained machine learning models can continue to improve and surpass that of numerical solvers [28, 29].

Local-FNO offers valuable insights in designing more accurate and efficient machine learning mod-

els. By leveraging local Fourier features, it effectively addresses three challenges often encountered with global Fourier features in high-resolution data: blurry output quality, extensive GPU memory usage, and substantial data demands. For a given number of Fourier modes, those defined over smaller local regions have shorter wavelengths, enabling the representation of finer-scale details. Local Fourier features also better capture spatially varying, non-stationary high-frequency information, similar to the improvements wavelet analysis brings over traditional Fourier analysis [67]. By dividing full-domain microclimate prediction into independent subtasks, Local-FNO reduces memory usage and improves scalability, opening the door for large-scale predictions across multiple GPUs. Training on local patches allows Local-FNO to make efficient use of limited data, enhancing generalization. Furthermore, geometry encoding introduces local geometric information, enabling the model to handle fluid dynamics across different geometric boundaries with greater precision. Patch overlapping enables interaction between neighboring regions, reducing discontinuities between patches.

This work has several limitations. First, Local-FNO is trained and tested in a single city area with a fixed wind profile. Although it can predict wind dynamics across different local building geometries within this area, its performance in other city areas and under varied wind profiles requires further study. Second, Local-FNO does not account for global wind field features, which works well for predicting small-scale turbulence in fully developed wind fields. However, the local training strategy can be less effective when significant large-scale patterns change in the global wind field. Third, patch overlapping in Local-FNO leads to some wind field grid data being trained and predicted multiple times, increasing computational time. A 20% overlap rate, for instance, results in approximately 144% of the computational time compared to non-overlapping training.

For future work, a promising direction is to integrate the strengths of global and local Fourier features. Global Fourier features can capture large-scale, low-frequency patterns, while local Fourier features can capture small-scale, high-frequency patterns. This approach could yield a model proficient in capturing both large-scale and small-scale dynamics within complex multiscale flow fields. Another avenue worth exploring is the coupling of CFD solvers with machine learning models. From a frequency perspective, CFD solvers converge more quickly on local, high-frequency features, while machine learning models converge more quickly on global, low-frequency features. Together, they could achieve faster computa-

tions without compromising accuracy.

References

1. Delmastro, C. & Chen, O. Buildings - Energy System - IEA.
2. Sezer, N. *et al.* Urban microclimate and building energy models: A review of the latest progress in coupling strategies. *Renew. Sustain. Energy Rev.* **184**, 113577, DOI: <https://doi.org/10.1016/j.rser.2023.113577> (2023).
3. Hong, T. *et al.* Urban microclimate and its impact on building performance: A case study of san francisco. *Urban Clim.* **38**, 100871, DOI: <https://doi.org/10.1016/j.uclim.2021.100871> (2021).
4. Bernard, J., Musy, M., Calmet, I., Bocher, E. & Keravec, P. Urban heat island temporal and spatial variations: Empirical modeling from geographical and meteorological data. *Build. Environ.* **125**, 423–438, DOI: <https://doi.org/10.1016/j.buildenv.2017.08.009> (2017).
5. Sun, H. *et al.* Pollutant cross-transmission in courtyard buildings: Wind tunnel experiments and computational fluid dynamics (cfd) evaluation. *Build. Environ.* **264**, 111919, DOI: <https://doi.org/10.1016/j.buildenv.2024.111919> (2024).
6. Klok, L., Zwart, S., Verhagen, H. & Mauri, E. The surface heat island of rotterdam and its relationship with urban surface characteristics. *Resour. Conserv. Recycl.* **64**, 23–29, DOI: <https://doi.org/10.1016/j.resconrec.2012.01.009> (2012). Climate Proofing Cities.
7. Sun, H. *et al.* Pollutant cross-transmission in courtyard buildings: Wind tunnel experiments and computational fluid dynamics (cfd) evaluation. *Build. Environ.* **264**, 111919, DOI: <https://doi.org/10.1016/j.buildenv.2024.111919> (2024).
8. Kanda, I. & Yamao, Y. Passive scalar diffusion in and above urban-like roughness under weakly stable and unstable thermal stratification conditions. *J. Wind. Eng. Ind. Aerodyn.* **148**, 18–33 (2016).
9. Marucci, D. & Carpentieri, M. Stable and convective boundary-layer flows in an urban array. *J. Wind. Eng. Ind. Aerodyn.* **200**, 104140 (2020).
10. Yang, S., Wang, L. L., Stathopoulos, T. & Marey, A. M. Urban microclimate and its impact on built environment – a review. *Build. Environ.* **238**, 110334, DOI: <https://doi.org/10.1016/j.buildenv.2023.110334> (2023).

11. Yang, S. *Assessment of Urban Microclimate and Its Impact on Outdoor Thermal Comfort and Building Energy Performance*. Ph.D. thesis, Concordia University (2024).
12. Katal, A., Mortezaazadeh, M. & Wang, L. L. Modeling building resilience against extreme weather by integrated cityffd and citybem simulations. *Appl. Energy* **250**, 1402–1417 (2019).
13. Mortezaazadeh, M., Wang, L. L., Albettar, M. & Yang, S. Cityffd – city fast fluid dynamics for urban microclimate simulations on graphics processing units. *Urban Clim.* **41**, 101063, DOI: <https://doi.org/10.1016/j.uclim.2021.101063> (2022).
14. Mortezaazadeh, M. & Wang, L. An adaptive time-stepping semi-lagrangian method for incompressible flows. *Numer. Heat Transfer, Part B: Fundamentals* **75**, 1–18 (2019).
15. Mortezaazadeh, M. & Wang, L. Slac—a semi-lagrangian artificial compressibility solver for steady-state incompressible flows. *Int. J. Numer. Methods for Heat & Fluid Flow* **29**, 1965–1983 (2019).
16. Mortezaazadeh, M. & Wang, L. L. Solving city and building microclimates by fast fluid dynamics with large timesteps and coarse meshes. *Build. Environ.* **179**, 106955 (2020).
17. Tian, G., Conan, B. & Calmet, I. Turbulence-Kinetic-Energy Budget in the Urban-Like Boundary Layer Using Large-Eddy Simulation. *Boundary-Layer Meteorol.* **178**, 201–223 (2021).
18. Tominaga, Y. & Stathopoulos, T. CFD simulation of near-field pollutant dispersion in the urban environment: A review of current modeling techniques. *Atmospheric Environ.* **79**, 716–730 (2013).
19. Ramponi, R., Blocken, B., de Coo, L. B. & Janssen, W. D. CFD simulation of outdoor ventilation of generic urban configurations with different urban densities and equal and unequal street widths. *Build. Environ.* **92**, 152–166 (2015).
20. Tian, G., Ma, Y., Chen, Y., Wan, M. & Chen, S. Impact of urban canopy characteristics on turbulence dynamics: Insights from large eddy simulation. *Build. Environ.* **250**, 111183 (2024).
21. Barlow, J. F. Progress in observing and modelling the urban boundary layer. *Urban Clim.* **10**, 216–240 (2014).
22. Blocken, B. 50 years of Computational Wind Engineering: Past, present and future. *J. Wind. Eng. Ind. Aerodyn.* **129**, 69–102 (2014).
23. Raissi, M., Perdikaris, P. & Karniadakis, G. E. Physics-informed neural networks: A deep learning framework for solving forward and inverse problems involving nonlinear partial differential equa-

- tions. *J. Comput. physics* **378**, 686–707 (2019).
24. Karniadakis, G. E. *et al.* Physics-informed machine learning. *Nat. Rev. Phys.* **3**, 422–440 (2021).
 25. Azizzadenesheli, K. *et al.* Neural operators for accelerating scientific simulations and design. *Nat. Rev. Phys.* 1–9 (2024).
 26. Lu, L., Jin, P., Pang, G., Zhang, Z. & Karniadakis, G. E. Learning nonlinear operators via deeponet based on the universal approximation theorem of operators. *Nat. machine intelligence* **3**, 218–229 (2021).
 27. Hao, Z. *et al.* Gnot: A general neural operator transformer for operator learning. In *International Conference on Machine Learning*, 12556–12569 (PMLR, 2023).
 28. Bi, K. *et al.* Accurate medium-range global weather forecasting with 3d neural networks. *Nature* **619**, 533–538 (2023).
 29. Lam, R. *et al.* Learning skillful medium-range global weather forecasting. *Science* **382**, 1416–1421 (2023).
 30. Kochkov, D. *et al.* Neural general circulation models for weather and climate. *Nature* **632**, 1060–1066 (2024).
 31. LeCun, Y., Bottou, L., Bengio, Y. & Haffner, P. Gradient-based learning applied to document recognition. *Proc. IEEE* **86**, 2278–2324 (1998).
 32. Kipf, T. N. & Welling, M. Semi-supervised classification with graph convolutional networks. In *5th International Conference on Learning Representations, ICLR 2017, Toulon, France, April 24-26, 2017, Conference Track Proceedings* (OpenReview.net, 2017).
 33. Dosovitskiy, A. *et al.* An image is worth 16x16 words: Transformers for image recognition at scale. In *9th International Conference on Learning Representations, ICLR 2021, Virtual Event, Austria, May 3-7, 2021* (OpenReview.net, 2021).
 34. Li, Z. *et al.* Fourier neural operator for parametric partial differential equations. In *9th International Conference on Learning Representations, ICLR 2021, Virtual Event, Austria, May 3-7, 2021* (OpenReview.net, 2021).
 35. Pathak, J. *et al.* Fourcastnet: A global data-driven high-resolution weather model using adaptive fourier neural operators. *arXiv preprint arXiv:2202.11214* (2022).

36. Li, Z., Peng, W., Yuan, Z. & Wang, J. Long-term predictions of turbulence by implicit u-net enhanced fourier neural operator. *Phys. Fluids* **35** (2023).
37. Rashid, M. M., Pittie, T., Chakraborty, S. & Krishnan, N. A. Learning the stress-strain fields in digital composites using fourier neural operator. *Iscience* **25** (2022).
38. Li, B., Wang, H., Feng, S., Yang, X. & Lin, Y. Solving seismic wave equations on variable velocity models with fourier neural operator. *IEEE Transactions on Geosci. Remote. Sens.* **61**, 1–18 (2023).
39. Gopakumar, V. *et al.* Plasma surrogate modelling using fourier neural operators. *Nucl. Fusion* **64**, 056025 (2024).
40. Kolmogorov, A. The Local Structure of Turbulence in Incompressible Viscous Fluid for Very Large Reynolds' Numbers. *Akademiia Nauk SSSR Doklady* **30**, 301–305 (1941).
41. Peng, W. *et al.* Fourier neural operator for real-time simulation of 3d dynamic urban microclimate. *Build. Environ.* **248**, 111063 (2024).
42. Wen, G., Li, Z., Azizzadenesheli, K., Anandkumar, A. & Benson, S. M. U-fno—an enhanced fourier neural operator-based deep-learning model for multiphase flow. *Adv. Water Resour.* **163**, 104180 (2022).
43. Ronneberger, O., Fischer, P. & Brox, T. U-net: Convolutional networks for biomedical image segmentation. In *Medical image computing and computer-assisted intervention–MICCAI 2015: 18th international conference, Munich, Germany, October 5-9, 2015, proceedings, part III 18*, 234–241 (Springer, 2015).
44. Liu, X., Xu, B., Cao, S. & Zhang, L. Mitigating spectral bias for the multiscale operator learning. *J. Comput. Phys.* **506**, 112944 (2024).
45. Ye, X., Li, H., Huang, J. & Qin, G. On the locality of local neural operator in learning fluid dynamics. *Comput. Methods Appl. Mech. Eng.* **427**, 117035 (2024).
46. Liu-Schiaffini, M. *et al.* Neural operators with localized integral and differential kernels. In *Forty-first International Conference on Machine Learning, ICML 2024, Vienna, Austria, July 21-27, 2024* (OpenReview.net, 2024).
47. Lippe, P., Veeling, B., Perdikaris, P., Turner, R. & Brandstetter, J. Pde-refiner: Achieving accurate long rollouts with neural pde solvers. *Adv. Neural Inf. Process. Syst.* **36** (2024).

48. Qin, S. *et al.* Toward a better understanding of fourier neural operators: Analysis and improvement from a spectral perspective. *arXiv preprint arXiv:2404.07200* (2024).
49. Mortezaazadeh, M. & Wang, L. L. A high-order backward forward sweep interpolating algorithm for semi-lagrangian method. *Int. J. for Numer. Methods Fluids* **84**, 584–597 (2017).
50. Zhan, D., Sezer, N., Hou, D., Wang, L. & Hassan, I. G. Integrating urban heat island impact into building energy assessment in a hot-arid city. *Buildings* **13**, DOI: [10.3390/buildings13071818](https://doi.org/10.3390/buildings13071818) (2023).
51. Luo, N. *et al.* A data schema for exchanging information between urban building energy models and urban microclimate models in coupled simulations. *J. Build. Perform. Simul.* 1–18 (2022).
52. Mortezaazadeh Dorostkar, M. *CityFFD–City Fast Fluid Dynamics Model for Urban Microclimate Simulations*. Ph.D. thesis, Concordia University (2019).
53. Kovachki, N., Lanthaler, S. & Mishra, S. On universal approximation and error bounds for fourier neural operators. *J. Mach. Learn. Res.* **22**, 1–76 (2021).
54. Li, Z. *et al.* Neural operator: Graph kernel network for partial differential equations. *arXiv preprint arXiv:2003.03485* (2020).
55. He, K., Zhang, X., Ren, S. & Sun, J. Deep residual learning for image recognition. In *Proceedings of the IEEE conference on computer vision and pattern recognition*, 770–778 (2016).
56. Tran, A., Mathews, A. P., Xie, L. & Ong, C. S. Factorized fourier neural operators. In *The Eleventh International Conference on Learning Representations, ICLR 2023, Kigali, Rwanda, May 1-5, 2023* (OpenReview.net, 2023).
57. Vaswani, A. Attention is all you need. *Adv. Neural Inf. Process. Syst.* (2017).
58. Cooley, J. W. & Tukey, J. W. An algorithm for the machine calculation of complex fourier series. *Math. computation* **19**, 297–301 (1965).
59. Li, Z., Huang, D. Z., Liu, B. & Anandkumar, A. Fourier neural operator with learned deformations for pdes on general geometries. *J. Mach. Learn. Res.* **24**, 1–26 (2023).
60. Rumelhart, D. E., Hinton, G. E. & Williams, R. J. Learning representations by back-propagating errors. *nature* **323**, 533–536 (1986).
61. Ruderman, D. & Bialek, W. Statistics of natural images: Scaling in the woods. *Adv. neural information processing systems* **6** (1993).

62. Osher, S. & Sethian, J. A. Fronts propagating with curvature-dependent speed: Algorithms based on hamilton-jacobi formulations. *J. computational physics* **79**, 12–49 (1988).
63. Courant, R., Friedrichs, K. & Lewy, H. Über die partiellen differenzengleichungen der mathematischen physik. *Math. annalen* **100**, 32–74 (1928).
64. Batchelor, G. K. *The theory of homogeneous turbulence* (Cambridge university press, 1953).
65. Tian, G. & Xiao, Z. Non-isothermal flow past a heated circular cylinder in subcritical regime: a numerical investigation based on large-eddy simulation. *J. Turbul.* **23**, 352–381 (2022).
66. Shannon, C. E. Communication in the presence of noise. *Proc. IRE* **37**, 10–21 (1949).
67. Daubechies, I. The wavelet transform, time-frequency localization and signal analysis. *IEEE transactions on information theory* **36**, 961–1005 (1990).